Open Access

Journal of Energy and Power Technology

LIDSEN Publishing Inc.

Original Research

Modeling of Autonomous Microgrid Operated at Medium-Voltage Level and at Constant Frequency and Study of Its Voltage Profile

Daming Zhang *

University of New South Wales, Sydney, Australia; E-Mail: daming.zhang@unsw.edu.au

* **Correspondence:** Daming Zhang; E-Mail: daming.zhang@unsw.edu.au

Academic Editor: Rodolfo Dufo-López

Journal of Energy and Power Technology
2023, volume 5, issue 1
doi:10.21926/jept.2301009

Received: December 06, 2022
Accepted: February 13, 2023
Published: February 17, 2023

Abstract

To increase power level in an autonomous microgrid, higher voltage is necessary. In this paper, detailed Matlab/Simulink modeling of a microgrid operated at medium-voltage level and at constant frequency has been conducted. Modified boost converter and medium-frequency transformer isolated DC/DC converter are adopted for both solar energy and wind energy harnessing in order for them to be connected with the microgrid. This paper further adopted a differential evolution (DE)-based method to carry out load flow analysis to work out the voltage at each bus. Results obtained from the DE method are nearly the same at some nodes or buses as those from Matlab/Simulink platform-based time-domain fixed-step modeling, while at other nodes they are very close to each other. Then DE method can be used to carry out load flow analysis in more complex microgrids with more nodes to overcome the limited modelling capability of Matlab/Simulink and other tools. Moreover, this new research effort also paves the way for the stability analysis of large-scale microgrids.

Keywords

AC microgrid; constant frequency; differential evolution; medium-frequency transformer; voltage profile

1. Introduction

As the depletion of fossil fuel is unstoppable, alternative power generations have been investigated extensively and intensively for many years. These solutions include biodiesel generation, solar energy-based generation, wind-based generation, geo-thermal energy-based generation, torrential water current based generation, hydropower generation, nuclear fission, and nuclear fusion generation etc. The accompanying storages include hydropower storage, battery storage, super-conducting magnetic energy storage, flying-wheel storage, compressed hydrogen storage, gravitational potential energy storage, and supercapacitor storage etc [1]. Here is a big issue: how to have a good combination of different generations and storages to bring in long-term benefit to human-beings and their living environment. Interest groups have been driving the directions strong headedly. Some directions may leave scar to our natural environment which will take years to recover, and to our health which may have no easy remedy to return for individuals.

The forming materials used in the system for harnessing wind energy, solar energy, geo-thermal energy, and torrential water energy are vastly available. So long proper environment awareness, health issues, retrieval and recycling of the used materials are well addressed, large-scale implementation of these energy harnessing system can be achieved.

As an example, PV panel is discussed here. The main forming ingredient of PV panels is made from sand which is vastly available. It seems that PV panels are the best choice. Nevertheless, some researchers reported that boron used in most PV panel fabrication has some gradual poisonous effects to human-beings, animals, and plants [2], less or no poisonous polarizing conductors for manufacturing PV panels are better choices. There are some alternatives available, such as gallium. Even so, each metal has potential of poison. Therefore, action needs to be taken such as using transparent cover to shield the PV panels. Even though there are some degrees of efficiency degradation, environment and human-beings' welfare of long-term will not be compromised. By doing so, widespread adoption of PV panels is a feasible choice to increase renewable energy harnessing.

Microgrid systems are good choices for increasing penetration levels of renewable energy generation. They can either operate in grid-tied mode or stand-alone mode. For the grid-tied operation, direct integration of inverters outputting a current at fixed frequency with the conventional synchronous generators has been investigated by some researchers [3]. This is one type of grid-tied operation. For such a type and other types of grid-connected operations, with the increase of renewable penetration level, stability of the overall large power system becomes a serious issue. Recently there are more cases of power outage and failure. Investigation is ongoing to seek answers on whether this is due to the increased penetration level.

Besides the grid-tied operation for the microgrids, off-grid or islanded or autonomous operation is also under intensive research. The control for operating the islanded microgrid includes both *f*-P, V-Q and V-P, *f*-Q methods [4-8]. Each one has pro and cons. Some researchers continue to show interest in further improving these methods.

Another proper method to manage an autonomous microgrid is to divide it into several regions, each region being installed with either conventional synchronous generators or renewable energy generation. Back-to-back converter or solid-state transformers in parallel are adopted to inter-connect neighboring regions. Conventional *f*-P and V-Q droop control is adopted for sharing real

and reactive power among multiple synchronous generators while a fixed-frequency or constant-frequency method is adopted for controlling the region installed with the inverter based renewable energy generation as described in [9-12].

In comparison, both *f*-P, V-Q and V-P, *f*-Q methods need to manage both frequency variation and voltage variation. In contrast, fixed-frequency or constant-frequency method only manages the voltage in the system, and the frequency in the system takes a constant value. Therefore, it is easier to manage the operation of the microgrid and shows better power quality of frequency.

In the previous research conducted by the author and his team, quite several aspects of the constant frequency operated microgrid have been examined [9-12]. In this new effort, some other un-tackled aspects have been investigated. These include 1) different forms of equivalent DC sources for the inverters; 2) load flow analysis or voltage profile calculation; 3) integration of gravitational energy storage in the large-scale microgrid.

The remaining contents are arranged as follows: In Section II, Matlab/Simulink modeling of a microgrid system operated at medium voltage level will be discussed in detail; Section III shows the power flow analysis for the autonomous microgrid; Section IV discusses energy storage in large-scale microgrid; Section V concludes the paper.

2. Matlab/Simulink Modeling of a Microgrid System

To cope with high-power demand from loads, a fundamental microgrid system shown in Figure 1 can be adopted, where inverters operate at relatively high voltage [10]. In such a system, there must be negative-sequence current compensators as shown in Figure 1 and Figure 2 to meet power demand by both three-phase and single-phase loads at the end users [13, 14]. This system can be designed to operate in both grid-connected mode and off-grid mode. By doing so, during rainy days or no-wind days, grid-connected operation is made possible. The power grid could be nation-wide one or could be just formed by locally located multiple synchronous generators.

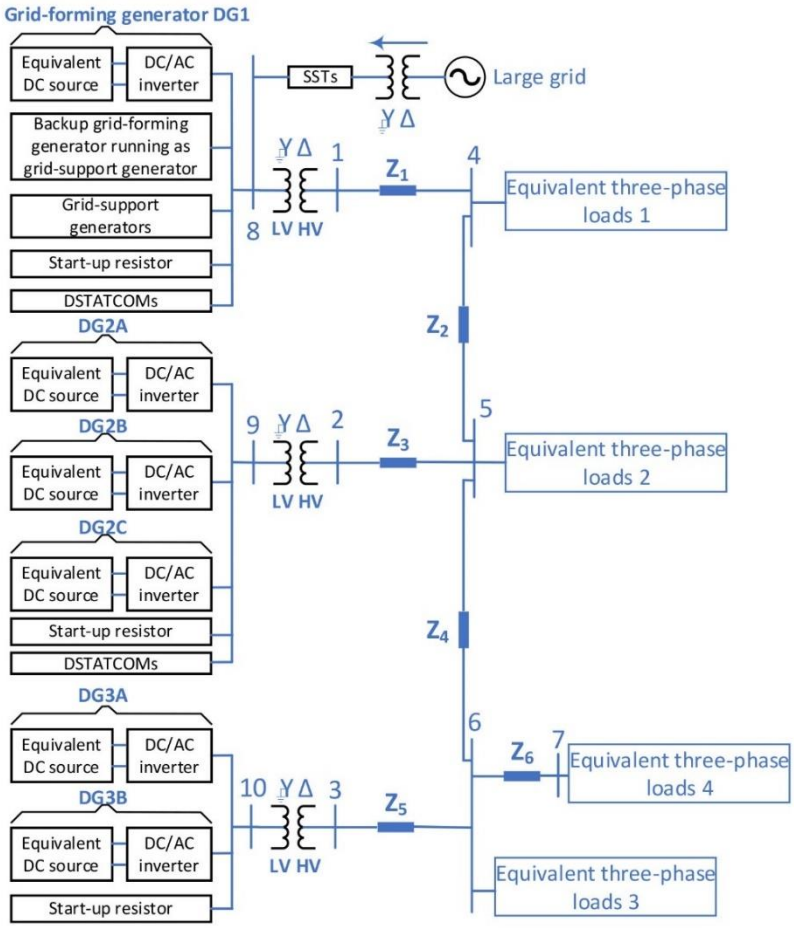

Figure 1 A large-scale microgrid.

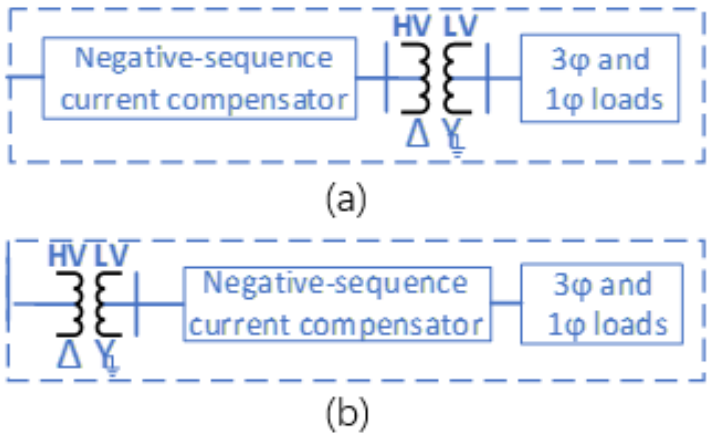

Figure 2 Negative-sequence current compensator for unbalanced load.

In such an autonomous microgrid in Figure 1, there is one grid-forming generator which is DG1 in this study, and there could be multiple grid-supporting generators and multiple grid-feeding generators. Although there are only two clusters of inverter-based grid-supporting and/or grid-feeding generators as indicated by DG2x and DG3x in Figure 1, for a practical application, there can be more than two clusters. Each cluster can be just a collection of several grid-supporting generators or a collection of several grid-feeding generators or a combination of these two kinds

of generators. As discussed in [9], it is necessary to have a back-up grid-forming generator, which operates as grid-supporting generator under normal operating condition. It can be located locally or remotely as discussed in [9]. Local one provides more reliable and smoother take-over of the grid-forming role in case that the main grid-forming generator becomes faulty. To ensure accurate tracing of the power reference for relatively low power factor system, DSTATCOMs need to be used together with the grid-forming generator. Furthermore, it is good to use a small local load together with each inverter. Such loads should be connected between LCL or LC filter and the breaker, especially for the grid-forming generator. By doing so, even under emergency condition, protection becomes easier.

One of the main advantages for the proposed control method over the autonomous microgrid is that it allows a sudden switch-in of heavy loads. Nevertheless, extra measure needs to be exerted to avoid system failure when there is heavy load being switched off [9-12]. This is because such a switch-off could cause the grid-forming generator running into absorbing real power. If this situation had happened for quite several cycles, the grid-forming generator would fail to take the grid-forming role, and the system would collapse. This was stated in the earlier publication by the author. One solution is to have a good communication among different DGs. When there is a sudden switch-off of heavy loads, command from the grid-forming generator is sent to the grid-supporting and grid-feeding generators to reduce their necessary outputs. Therefore, it is always good to install another grid-supporting generator with the grid-forming generator as shown in [9]. That is to say, the back-up grid-forming generator which runs as grid-supporting generator can be controlled to output real power under normal operation condition. When the sudden switch-off of heavy loads occurs, this grid-supporting generator is to reduce its real power and reactive power output significantly. By doing so, the grid-forming generator continues to output positive real power. Other than the back-up grid-forming generator, extra grid-supporting generators can be designed to allow bi-directional power flow, under very light loading condition, the accompanying grid-supporting generator can even absorb real power and reactive power. Another alleviating measure is to connect a small load or start/stop resistive load between the LCL or LC filter and the breaker for the grid-forming generator.

The equivalent DC sources for the inverters in Figure 1 can take different forms, some of which are shown in Figure 3. One can see that conventional generators can be used to supply power to their local loads and can also be used to be the DC source of the inverter through AC/DC rectifier. As discussed earlier by the author that the real power from the grid-forming generator can be set to be a fixed value, power converted from synchronous generators through rectifier and passed through the grid-forming inverter can be constant or nearly constant. Although battery storage has attracted high interest for storing energy in power system in recent years, other solutions are still available, e.g. gravitational potential energy storage [15-20]. As shown in Figure 3c, such gravitational potential energy storage systems together with super-capacitors buffer can be used as equivalent DC source. As multiple units can be used to even off power dis-continuity due to start-stop of machines in the system, less super-capacitors need to be used. Figure 3d and Figure 3e show the PV-based and wind-based generation to serve as the equivalent DC source. To boost the voltage from solar and wind generation high enough to be interfaced with the microgrid, a modified boost converter and medium-frequency transformer isolated DC/DC converter are interconnected to achieve this purpose. Such renewable energy harnessing systems can work in MPPT mode or power curtailment mode [10]. By controlling the inductor current in the modified

boost converter, PV system can operate flexibly in the curtailment mode for the microgrid voltage management. This comes with a compromise that more PV panels need to be used. Other sources like torrential water current-based system or batteries can also be used as the equivalent DC sources. In this paper, some of the equivalent DC sources as shown in Figure 3 are used in the microgrid.

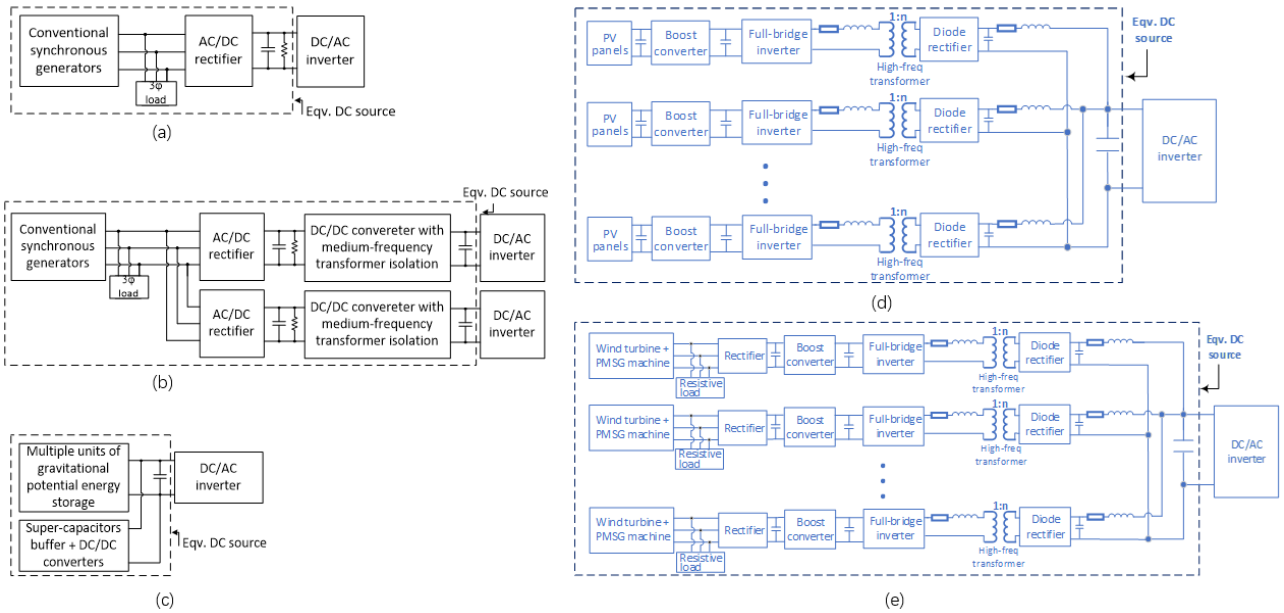

Figure 3 Different forms of equivalent DC sources.

In this study, a reduced autonomous microgrid system from that in Figure 1 is taken. It is shown in Figure 4 where DG1A serves as the grid-forming generator while DG1B serves as the reactive power compensator. DG2 and DG3 are either the grid-supporting or grid-feeding generators. The ratio of each transformer in Figure 4a are 4.5 kV/22 kV (Inverter side/transmission line side, LL rms). For other studies, the ratios of these transformers could be different from each other when the rated voltages at the inverters' side are different. At load side, the ratio of each transformer is the same and equal to 22 kV/415 V. In Figure 4a, loads are referred to 22 kV side.

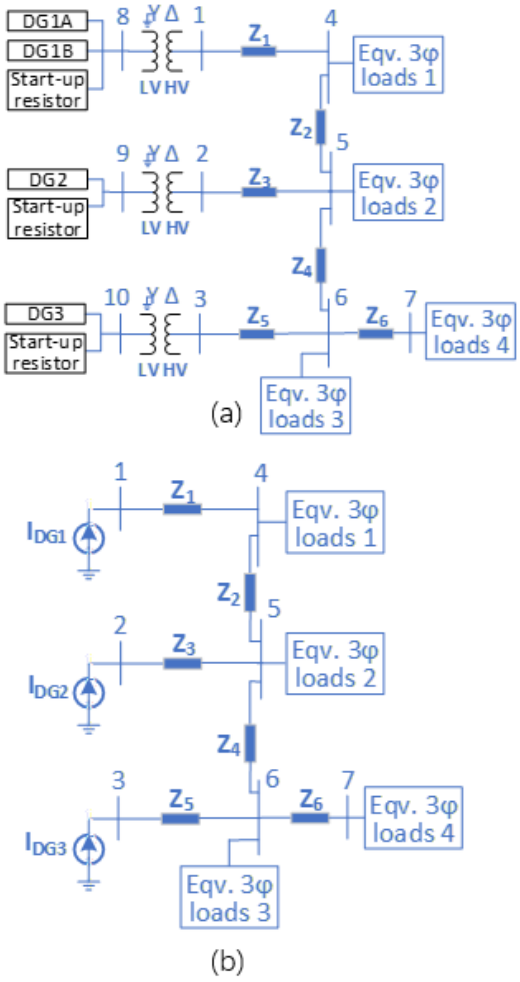

Figure 4 A reduced autonomous microgrid under study.

As proposed in [9-12], each DG in the microgrid works in current-controlled mode. Then a simplified model for the system in Figure 4a is obtained and shown in Figure 4b, where the current I_{DG1} for DG1 is the equivalent of the combination of DG1A and DG1B in Figure 4a, and the series impedances of 4.5 kV/22 kV transformers are combined with their respective inter-connection line impedances. The reference current for each DG is produced by the formulas (1) through (4) [8-12]. More details are given in Appendix A.

$$\begin{bmatrix} V_{dp} \\ V_{qp} \\ V_{0p} \end{bmatrix} = (2/3) \begin{bmatrix} \cos\theta & \cos(\theta - 2\pi/3) & \cos(\theta + 2\pi/3) \\ -\sin\theta & -\sin(\theta - 2\pi/3) & -\sin(\theta + 2\pi/3) \\ 1/2 & 1/2 & 1/2 \end{bmatrix} \begin{bmatrix} v_a \\ v_b \\ v_c \end{bmatrix} \tag{1}$$

$$\begin{bmatrix} I_d^* \\ I_q^* \end{bmatrix} = \frac{1}{V_d^2 + V_q^2} \begin{bmatrix} V_d & V_q \\ V_q & -V_d \end{bmatrix} \begin{bmatrix} \mathrm{P_{ref}} \\ Q_{\mathrm{Ref}} \end{bmatrix} \tag{2}$$

where $V_d = V_{dp}/\sqrt{2}$, $V_q = V_{qp}/\sqrt{2}$, $\mathrm{P_{ref}}$ and $\mathrm{Q_{ref}}$ are one-phase power, and $\theta = angle(v_a)$. Therefore, I_d^* and I_q^* are in rms values.

$$\begin{bmatrix} i_{\mathrm{a}}^{*} \\ i_{\mathrm{b}}^{*} \\ i_{\mathrm{c}}^{*} \end{bmatrix} = \sqrt{2} \cdot x \cdot \begin{bmatrix} \cos\theta & -\sin\theta \\ \cos(\theta - 2\pi/3) & -\sin(\theta - 2\pi/3) \\ \cos(\theta + 2\pi/3) & -\sin(\theta + 2\pi/3) \end{bmatrix} \begin{bmatrix} I_d^{*} \\ I_q^{*} \end{bmatrix} \tag{3}$$

$$\begin{bmatrix} i_{\mathrm{a}}^{*} \\ i_{\mathrm{b}}^{*} \\ i_{\mathrm{c}}^{*} \end{bmatrix} = \frac{\sqrt{2}}{V_d^2 + V_q^2} \begin{bmatrix} \cos\theta & -\sin\theta \\ \cos(\theta - 2\pi/3) & -\sin(\theta - 2\pi/3) \\ \cos(\theta + 2\pi/3) & -\sin(\theta + 2\pi/3) \end{bmatrix} \begin{bmatrix} V_d & V_q \\ V_q & -V_d \end{bmatrix} \begin{bmatrix} x\mathrm{P}_{\mathrm{ref}} \\ xQ_{\mathrm{Ref}} \end{bmatrix} \tag{4}$$

where x takes a value of 100%. When it takes value slightly different from 100%, $\mathrm{P}_{\mathrm{ref}}$ and $\mathrm{P}_{\mathrm{output}}$ have difference. Nevertheless, this does not influence the system to operate stably in the numerical modeling as the grid-forming generator and its accompanying DSTATCOM can process the shortage of real and reactive power automatically to meet KCL. In the following study, it is set to 100%. In the hardware experiment, it is better to use 100%.

Here two cases will be studied. In the first case, DG1 and DG2 are powered by an ideal DC source while DG3 is powered by four paralleled identical units of PV based renewable generation as shown in Figure 3d with the total real power of DG3 from PV panel equal to 644.2 kW. In the second case, DG1 is powered by an ideal DC source while DG2 is powered by three paralleled identical units of wind based renewable generation as shown in Figure 3e and DG3 is still powered by PV panels, same as that in Case 1. The total real power of DG3 from PV panels is equal to 678.2 kW while the total real power of DG2 from wind generation is equal to 235.5 kW in the second case.

As can be seen in Figure 3d and Figure 3e, there are common parts for the two systems: modified boost converter + medium-frequency transformer isolated DC/DC converter. As discussed in [21], a universal controller can be used to control the modified boost converter for harnessing wind energy and solar energy. Its control flow is shown in Figure 5, where the transfer function as given by Eqn. (5) is used. Eqn. (6) together with (5) can be used to implement double loop control. Nevertheless, from numerous numerical experimenting, it is found that the control method as shown in Figure 5 is a better choice. Eqns. (5) and (6) are derived from the circuits as shown in Figure 6.

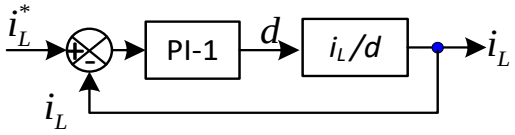

Figure 5 Inductor current control for the modified boost converter.

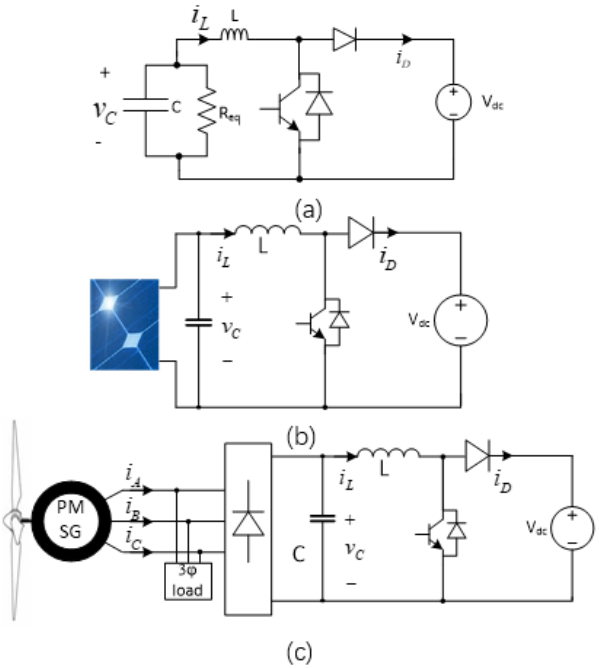

Figure 6 (a) Modified boost converter; (b) Modified boost converter with solar panel; (c) Modified boost converter with wind based generation.

$$\left.\frac{\hat{\imath}_L(s)}{\hat{d}(s)}\right|_{\hat{v}_{dc}(s)=0} = \frac{s+\frac{1}{RC}}{s^2+\frac{1}{RC}s+\frac{1}{LC}} \cdot \frac{\bar{V}_{dc}}{L} \tag{5}$$

$$\left.\frac{\hat{v}_c(s)}{\hat{d}(s)}\right|_{\hat{v}_{dc}(s)=0} = \frac{1}{s^2+\frac{1}{RC}s+\frac{1}{LC}} \cdot \left(\frac{-\bar{V}_{dc}}{LC}\right) \tag{6}$$

Table 1 shows the parameters used for the modified boost converter for both solar energy and wind energy harnessing. One can see that for the solar energy harnessing, capacitance needs to be small while for the wind generation usage, capacitance needs to be large enough.

Table 1 Parameters of the modified boost converter for PV panel and wind generation.

Parameters	Values for PV	Values for Wind
L	1.2 mH	1.2 mH
C	0.5 mF	5.0 mF
fswitching	5 kHz	5 kHz
fsampling	100 kHz	100 kHz

Table 2 lists the parameters for each inverter in the system as shown in Figure 4a. The switching frequency of each inverter is chosen to be 4 kHz. By doing so, the market available TI-28379D microcontroller can be adopted to control the inverter. As lower switching frequency is taken to overcome the low speed of ADC and limited calculation power in microcontroller, this results in a compromise that greater inductance needs to be used. When the higher-speed ADC and more capable microcontroller are available, it is better to use higher switching frequency to

reduce inductance. Furthermore, for reliable operation, it is better to use higher sampling frequency. Another solution is to transmit the three reference voltages from one TI-28379X to another one via DAC-ADC interface, in which higher EPWM interrupt frequency, e.g. 480kHz can be taken, though the sampling frequency and references' update in the first TI-28379X could be as low as 80kHz. By doing so, the references are compared with a code-produced triangular carrier waveform with 480kHz/4kHz=120 points over one cycle of switching frequency 4kHz. For low switching frequency operation, it is necessary to consider the Barkhausen effect in the magnetic materials as it could produce noise and cause system malfunction. Nano-crystalline based magnetic inductors could avoid this from happening.

Table 2 Parameters for each inverter.

Parameters	Values
L_{1inv}	22.5 mH
C_{inv}	25 μF
L_{2inv}	4.5 mH
$R_{damping}$	1 Ω
fswitching	4 kHz
K_p	0.275
K_i	40.0
K	80.5
$f_{sampling}$	100 kHz
K_{v0}	2000 (Phase-voltage rms value is used for P_{ref} generation)
K_v	1.15
K_{pq}	0.4843

Table 3 shows the information of loads. In this study, the P and Q values of the loads are converted into *R* and *L* values for each load by using

$$R = \frac{3V^2}{P \cdot \left(1 + K_{QP}^2\right)} \tag{7}$$

$$L = \frac{3V^2 \cdot K_{QP}}{2\pi \cdot 50 \cdot P \cdot \left(1 + K_{QP}^2\right)} \tag{8}$$

where $K_{QP} = Q/P$ and *V* is the rms value of the phase voltage.

Table 3 Different loads.

	Load 1	Load 2	Load 3	Load 4
P (kW)	400	500	400	400
Q (kVAr)	300	350	250	250
On/off state	Initial: off Turn-On: 2 s	Always on	Always on	Initial: off Turn-on: 3.5 s

Table 4 shows the resistance and inductance of each line at 22 kV side.

Table 4 Parameters of lines.

	Line1	Line2	Line3	Line4	Line5	Line6
R (Ω)	8.15	9.75	12.75	12.25	12.45	12.95
L (mH)	4.0	5.25	4.75	4.25	3.50	5.15

Results for Case 1 are shown in Figures 7 through 9. In Figure 7, the variable irradiance is shown and the inductor currents in the modified boost converter for each of four identical units as shown in Figure 3d are also given. One can see that current change traces its reference and the irradiance changes quite well.

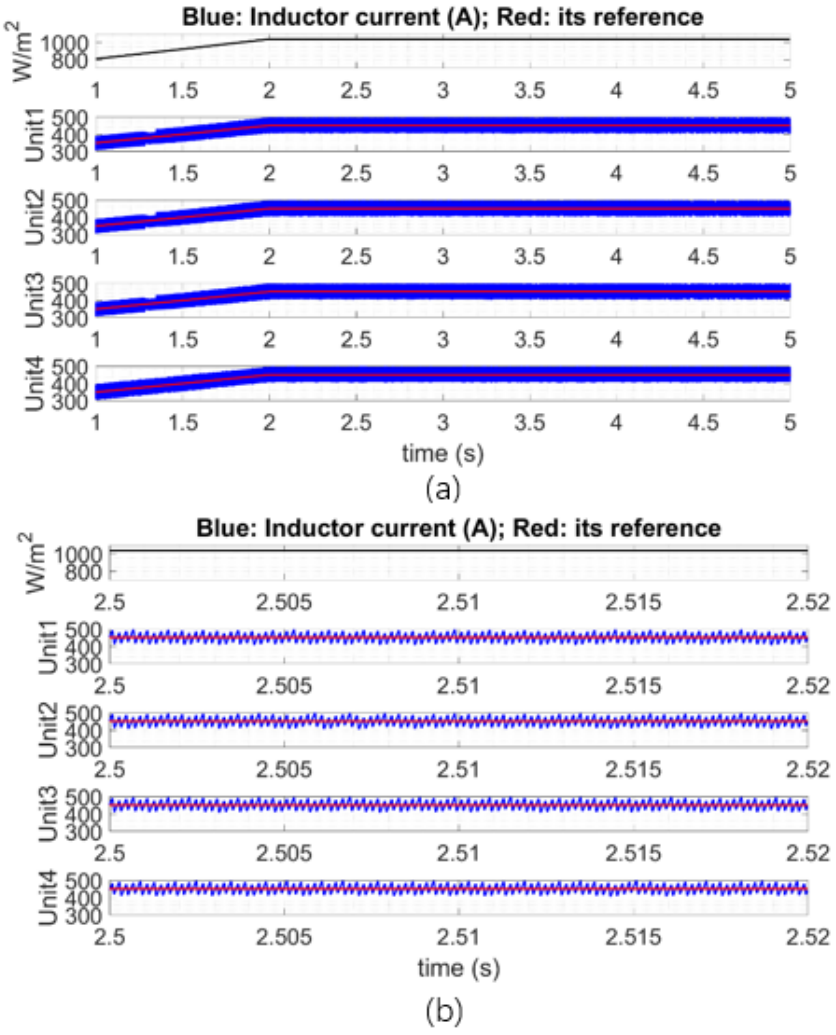

Figure 7 Irradiance and inductor currents.

Figure 8 shows the DC voltages at different locations in each of the four identical converter circuits in Figure 3d. The top sub-plot in Figure 8 shows the terminal voltage at each PV panel, the middle sub-plot shows the voltage at the output of the modified boost converter while the bottom sub-plot shows the voltage across the capacitor at the input of each inverter. In this case, the full-

bridge inverters in Figure 3d are controlled to regulate the output voltages of the modified boost DC/DC converters to settle down at the targeted values. From them, one can see that each of the modified boost converter and medium-frequency transformer isolated DC/DC converter boosts the voltage significantly. Overall, the voltage is increased from around 600 V to around 8500 V.

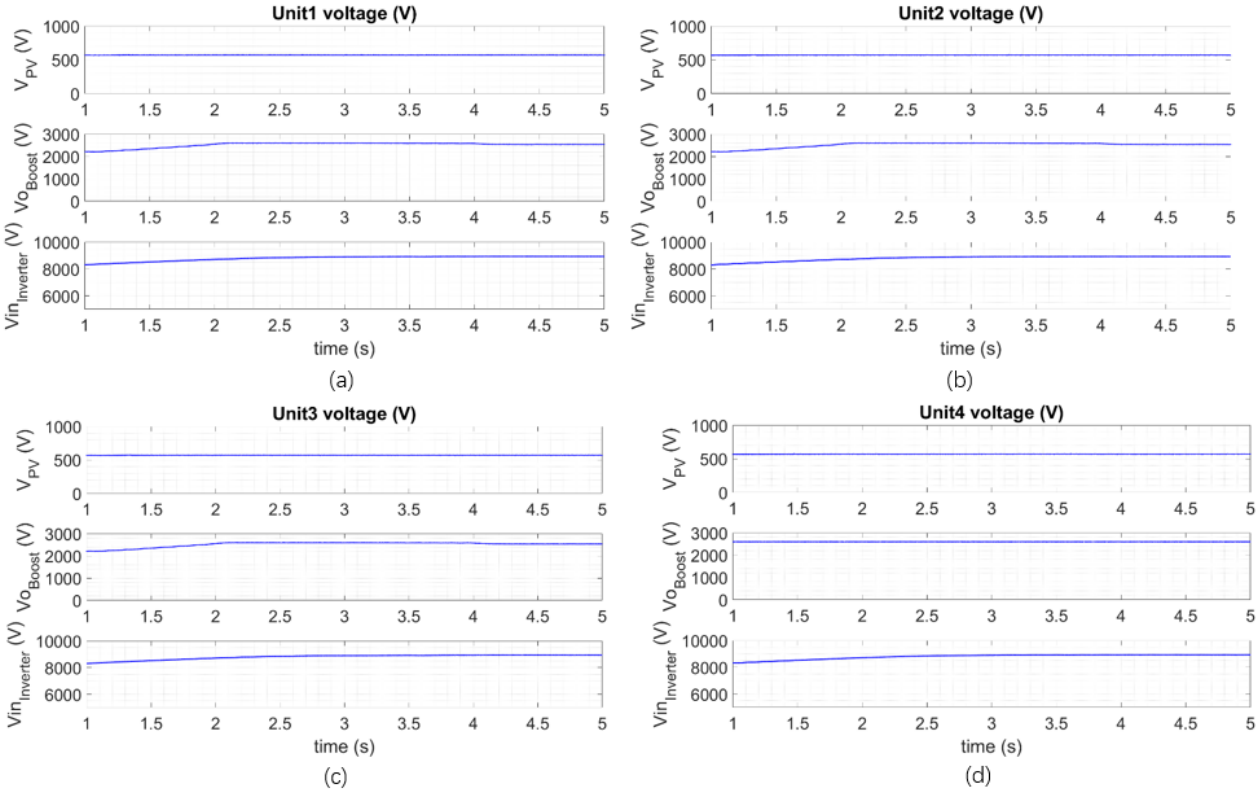

Figure 8 DC voltages at different locations in Figure 3d for Case 1.

Figure 9 show the real power and reactive power outputs and their references from each of DG1, DG2 and DG3. For both DG2 and DG3, the output real and reactive power traces their respective references accurately. For DG1, its reactive power traces its reference also accurately. But there is a small difference between the real power output from DG1 and its reference. The difference is due to the interconnection resistance between DG1A, the grid-forming generator and DG1B, the accompanying DSTATCOM.

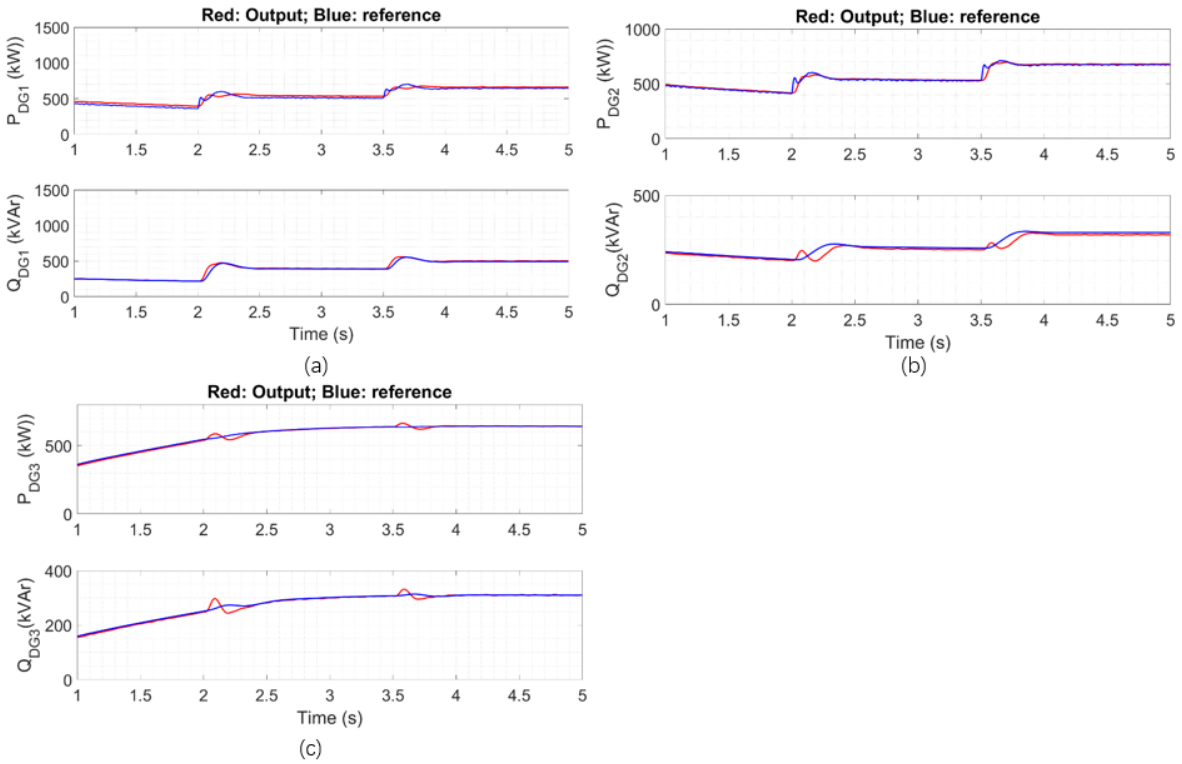

Figure 9 Power from each of DG1, DG2 and DG3 for Case 1.

Similar results of the real power and reactive power for Case 2 are shown in Figure 10, from which one can see that tracing is also very accurate.

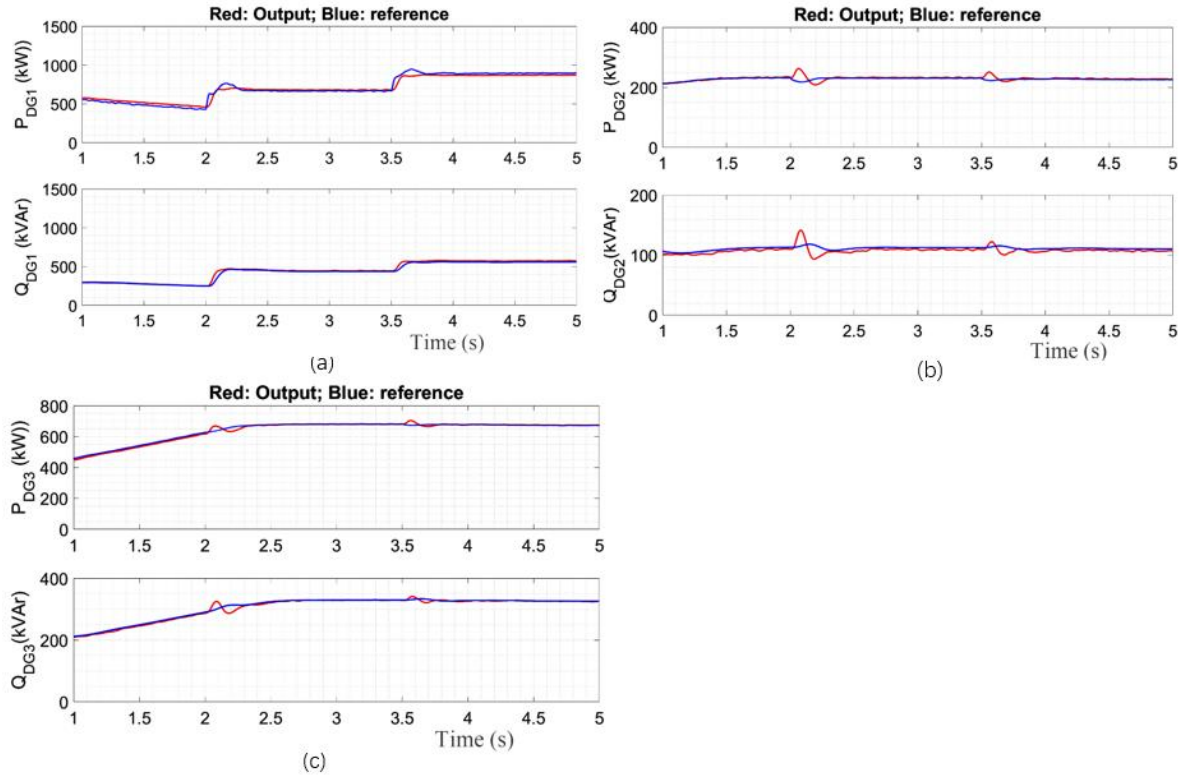

Figure 10 Power from each of DG1, DG2 and DG3 for Case 2.

3. Power Flow Analysis for the Autonomous Microgrid

Power flow analysis is necessary to investigate the voltage profiles in a power system [22]. For this study, a differential evolution-based method is adopted to carry out the power flow analysis in the autonomous microgrid system in Figure 4b.

The formulation for this purpose is shown in (9) through (19) for implementing differential evolution (DE)-based method [23, 24]. The DE method has the feature of global searching and convergence capability. It is widely used in optimization research.

From numerous modeling conducted earlier and also the ones shown in Figure 9 and Figure 10, it has been found that the proposed control method can have accurate tracing of real power and reactive power for both grid-forming generator and its accompanying DSTATCOM, grid-supporting generators and grid-feeding generators. Therefore, the real power output from each of the DG1, DG2 and DG3 can be expressed as follows, even though it is taken as reference power for each of them.

$$\mathrm{P}_{DG,j} = \left[\mathrm{P}_{DG,ref0,j} + \mathrm{K}_{V0,j} \cdot \left(\mathrm{K}_{V,j} \cdot V_{ref} - \left|\mathrm{V}_j\right|\right)\right]/3.0 \tag{9}$$

where j = 1, 2 and 3. The reason that a factor of 3 is used is to work out one-phase power for the following calculation. Similarly, both V_{ref} and V_j are in rms value for the following calculation. To make the calculation of voltage magnitude more accurate, a notch-filter-based bandpass filter could be applied to remove noises in the measured time-domain values.

Similarly, even though a percent times the measured output real power, not real power reference is used as the reactive power reference, with the accurate tracing, the following formula for one-phase reactive power can be established to be the reactive power output for both grid-supporting and grid-feeding generators.

$$Q_{DG,j} = K_{pq,j} \cdot P_{DG,j} \tag{10}$$

where j = 2, and 3. In this study $K_{pq,j}$ for each of DG2 and DG3 is set to 0.4843 as indicated in Table 2. As DG1 serves as the grid-forming generator and only outputs real power, the necessary reactive power is output from its accompanying DSTATCOM. So, the above equation is not necessary for it.

The method adopted here to produce real power and reactive power references is the same as that in [10] but is different from F1-F2 approach in [9, 12]. Both methods can achieve the targets of accurately tracing the real power and reactive power outputs. Nevertheless, for the case in which there are significant impedances between DGs due to being quite apart from each other, the method adopted in [10] and here could be a better choice.

According to KCL, the following equation can be established.

$$\frac{\mathrm{V}_j}{\mathrm{Z}_{L,j}} + \sum_{k=1,k\neq j}^{7} \frac{\mathrm{V}_j - \mathrm{V}_k}{\mathrm{Z}_{jk}} = \mathrm{I}_{DG,j} \tag{11}$$

where *j* = 1, 2, …, 7. For those nodes without loads, $Z_{L,j} = \infty$. For those nodes with direct link with another neighboring node, Z_{jk} is the line impedance between them while for those nodes without direct link, $Z_{jk} = \infty$. For the nodes without equivalent current source, $I_{DG,j} = 0$.

Between neighboring nodes, the following equation is established according to KVL.

$$V_j = V_{j,x} + jV_{j,y} = V_k + I_{jk}Z_{jk} \tag{12}$$

where *k* is a node neighboring to node *j* and Z_{jk} is the line impedance linking node *j* with node *k*.

For each equivalent current source indicated by I_{DG1}, I_{DG2}, and I_{DG3}, its real part and imaginary part can be expressed in terms of the voltage at the respective node and power from it as shown below.

$$I_{j,x} = \frac{P_{DG,j} \cdot V_{j,x} + Q_{DG,j} \cdot V_{j,y}}{V_{j,x}^2 + V_{j,y}^2} \tag{13}$$

$$I_{j,y} = \frac{P_{DG,j} \cdot V_{j,y} - Q_{DG,j} \cdot V_{j,x}}{V_{j,x}^2 + V_{j,y}^2} \tag{14}$$

where *j* = 1, 2, and 3 as these nodes have equivalent current source connected.

The complex power from either the grid-supporting generators or the grid-feeding generators DG2 and DG3 can be expressed as follows.

$$P_j + jQ_j = \left[\left(V_{k,x} + jV_{k,y}\right) + \mathrm{I}_j \times \mathrm{Z}_{j,k}\right] \cdot \mathrm{I}_j^* \tag{15}$$

where $I_j = I_{j,x} + jI_{j,y}$, $Z_{jk} = Z_{jk,x} + jZ_{jk,y}$; for bus 3, *j* = 3 and *k* = 6 while for bus 2, *j* = 2 and *k* = 5.

Equating the real parts and imaginary parts on two sides of (15), one can obtain

$$I_{j,x} = \frac{PQ_j - A_2 \cdot I_{j,y}}{A_1} \tag{16}$$

$$I_{j,y} = \frac{-C_2 - \sqrt{C_2^2 - 4C_1C_3}}{2C_1} \tag{17}$$

where

$C_1 = Z_{jk,x} + Z_{jk,x} \cdot \left(\frac{A_2}{A_1}\right)^2$, $C_2 = V_{k,y} - Z_{jk,x} \cdot \frac{2PQ_j \cdot A_2}{A_1} - V_{k,x} \cdot \frac{A_2}{A_1}$, $C_3 = V_{k,x} \cdot \frac{PQ_j}{A_1} - QP_j$;

$A_1 = V_{k,x} - k_{zk} \cdot V_{k,y}$, $A_2 = V_{k,y} + k_{zk} \cdot V_{k,x}$, $PQ_j = P_j - Q_j \cdot k_{zk}$;

$k_{zk} = \frac{Z_{jk,x}}{Z_{jk,y}}$; for bus 3, *j* = 3 and *k* = 6 while for bus 2, *j* = 2 and *k* = 5.

There are two objective functions defined which are given below.

$$\mathrm{Obj1} = \mathrm{Min}\left\{\left|P_{DG1,ref} - P_{DG1,calculated}\right|\right\} \tag{18}$$

$$\mathrm{Obj2} = \mathrm{Min}\left\{\sqrt{\left(V_{2,xa} - V_{2,xb}\right)^2 + \left(V_{2,ya} - V_{2,yb}\right)^2}\right\} \tag{19}$$

The results for Case 1 and Case 2 are shown in Table 5, from which one can see that for both cases, the DE based method and Matlab/Simulink-based real-time fixed-step method reach nearly the same results.

Table 5 Line-line peak voltage at each bus from both Simulink and DE method.

	Approach	V_1(kV)	V_2(kV)	V_3(kV)	V_4(kV)	V_5(kV)	V_6(kV)	V_7(kV)
Case 1	Simulink	31.53	31.59	31.35	29.63	29.33	29.54	29.16
	DE	31.62	31.35	31.11	31.18	30.93	30.69	30.33
Case 2	Simulink	29.98	29.36	29.62	28.05	27.55	27.84	27.50
	DE	30.00	30.40	29.69	31.18	30.93	29.34	29.03

4. Energy Storage in Large-scale Microgrids

As wind is highly intermittent and solar energy is only available during sunny days, it is necessary to use energy storage to store energy from solar and wind. That is to say, in the microgrid as shown in Figure 1, besides harnessing solar energy and wind energy directly by the grid-feeding generators, a separate DC microgrid needs to be constructed to convert solar energy and wind energy into the gravitational potential energy using the machine system as described in [15-20].

The machine systems in Figure 11 and Figure 12 show two possible gravitational potential energy storage with relatively high efficiency. To reduce the rigidity and mechanical strength requirement, width W1 in Figure 12 can be chosen to be short. For example, in one design, one can choose vertical height h of each stator layer to be 60cm while W1 is chosen to be 50 cm. Instead of lifting up or lowering down a pair of containers with a significant weight, for example 25 tons each, one can choose to use lighter ones in order to reduce the pressure on the side surfaces of the movers' vertical supporting poles, along which containers are moved through bearings' interface. To reduce the pressure on the support foundation, a total stator vertical height of around 60 m can be chosen. Several such identical units are used. As discussed in [17-19], distributed stator windings and multiple rotor structures can be taken. As shown in Figure 3c, multiple units of the machine systems as given in either Figure 11 or Figure 12 can be used to even off the power variation due to start/stop of some of the units. By using super-capacitors buffer, the output from such an equivalent DC source can be made smoother. As the machine system can move at different speed, variable power output can be obtained from it. By doing so, the DC microgrid control can be made easier. Furthermore, output power curtailment technique could be used to control solar and wind energy harnessing units in the DC microgrid to further facilitate its voltage control.

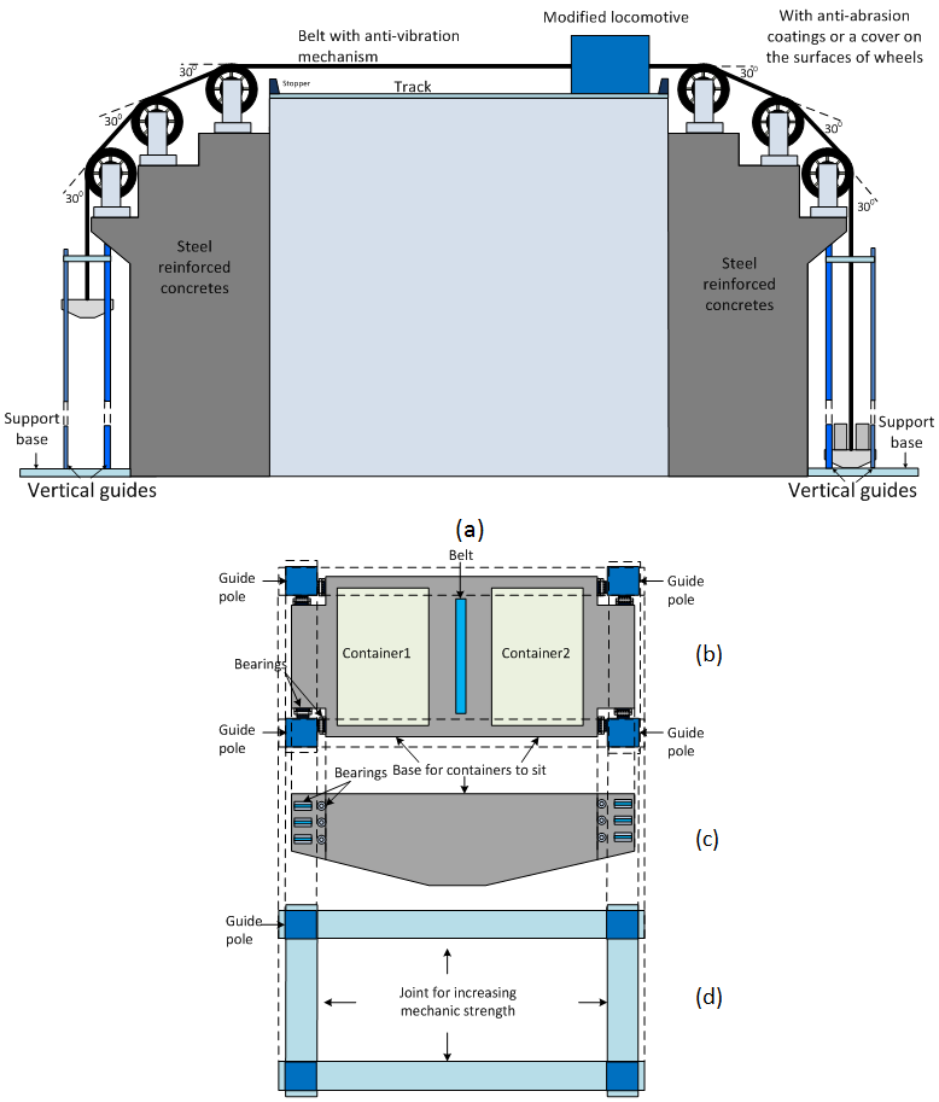

Figure 11 (a) Bi-directional lifting of containers with heavy masses; (b) Top view of the container holder with guide poles' support; (c) Side view of the container holder with bearings; (d) Joint at the top of the guide poles.

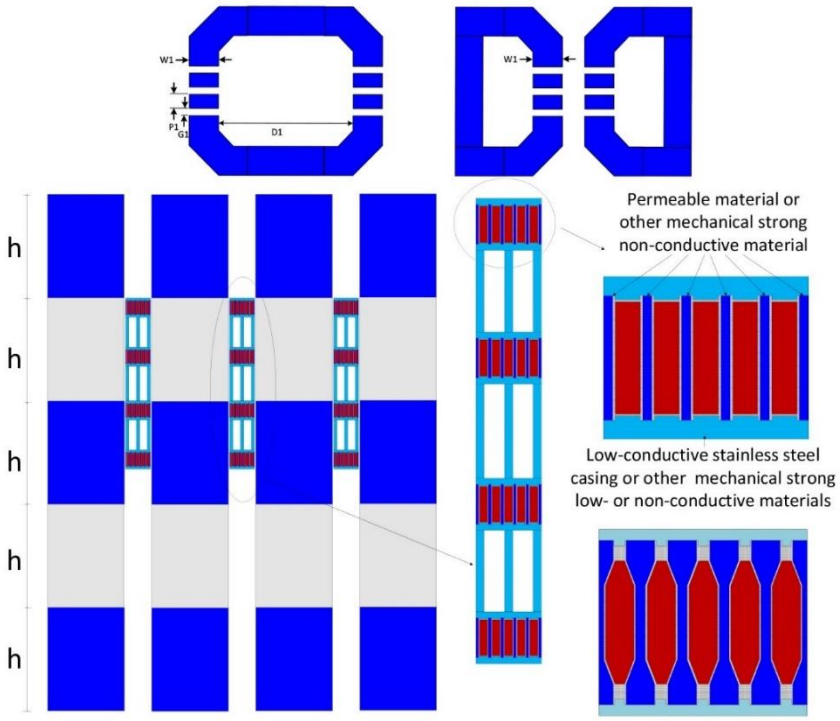

Figure 12 Some parts of the linear machine system with vertical movement.

5. Conclusions

This paper presents a comprehensive modeling of autonomous microgrid operated at medium-voltage and at constant or fixed frequency. Several equivalent DC sources and their roles for each inverter in the autonomous AC microgrid have been discussed in detail. Then multiple converters in parallel to harness solar and wind energy are incorporated into the AC microgrid system. Each of the multiple converters contains both the modified boost converter and medium-frequency transformer isolated DC/DC converter. The modified boost converter in the two systems share common control strategy. As medium-frequency transformers are used, the total boost factor is increased. Curtailment of power extraction from the renewable generation has been implemented to increase system voltage regulation flexibility. A differential evolution-based method has been taken to work out the voltage profiles in the autonomous AC microgrid. The numerical results are nearly the same as those from Matlab/Simulink-based real-time fixed-step approach. By doing so, for large microgrid which cannot be modelled in Matlab/Simulink, the proposed DE based method can be taken to carry out voltage profile calculation.

Appendix

Appendix A Comparison of two methods for working out current references

Method 1

The method 1 is the same as that described by equations (1) through (4) in the main context with x = 100% in (4).

Method 2

For power conservation, the following transform is usually adopted,

$$\begin{bmatrix} V_d \\ V_q \\ V_0 \end{bmatrix} = \sqrt{\frac{2}{3}} \begin{bmatrix} \cos\theta & \cos(\theta - 2\pi/3) & \cos(\theta + 2\pi/3) \\ -\sin\theta & -\sin(\theta - 2\pi/3) & -\sin(\theta + 2\pi/3) \\ 1/\sqrt{2} & 1/\sqrt{2} & 1/\sqrt{2} \end{bmatrix} \begin{bmatrix} v_a \\ v_b \\ v_c \end{bmatrix} \quad \text{(A1)}$$

$$\begin{bmatrix} I_d \\ I_q \end{bmatrix} = \frac{1}{V_d^2 + V_q^2} \begin{bmatrix} V_d & V_q \\ V_q & -V_d \end{bmatrix} \begin{bmatrix} \mathrm{P}_3 \\ Q_3 \end{bmatrix} \quad \text{(A2)}$$

where real and reactive powers are three-phase values.

Then

$$\begin{bmatrix} i_a \\ i_b \\ i_c \end{bmatrix} = \sqrt{\frac{2}{3}} \begin{bmatrix} \cos\theta & -\sin\theta \\ \cos(\theta - 2\pi/3) & -\sin(\theta - 2\pi/3) \\ \cos(\theta + 2\pi/3) & -\sin(\theta + 2\pi/3) \end{bmatrix} \begin{bmatrix} I_d \\ I_q \end{bmatrix} \quad \text{(A3)}$$

Although two methods result in different V_d, and different V_q, and also different I_d, and different I_q, one can verify that the final time-domain expressions for $i_a(t)$, $i_b(t)$ and $i_c(t)$ are the same.

Author Contributions

The author did all the research work of this study.

Competing Interests

The author has declared that no competing interests exist.

References

1. Mahlia TM, Saktisahdan TJ, Jannifar A, Hasan MH, Matseelar HS. A review of available methods and development on energy storage; technology update. Renew Sust Energ Rev. 2014; 33: 532-545.
2. Diez S, Vedde J, Shoulga YG, Vlasenko TV, Glunz SW, Warta W, et al. Alternatives to boron-doped Czochralski for silicon solar cell processing. Proceedings of the 19th European Photovoltaic Solar Energy Conference; 2004 June 7-11; Paris, France.
3. Zhang Z, Huang X, Jiang J, Wu B. A load-sharing control scheme for a microgrid with a fixed frequency inverter. Electr Power Syst Res. 2010; 80: 311-317.
4. Zhong QC. Robust droop controller for accurate proportional load sharing among inverters operated in parallel. IEEE Trans Ind Electron. 2013; 60: 1281-1290.
5. Olivares DE, Mehrizi-Sani A, Etemadi AH, Cañizares CA, Iravani R, Kazerani M, et al. Trends in microgrid control. IEEE Trans Smart Grid. 2014; 5: 1905-1919.
6. De Brabandere K, Bolsens B, Van den Keybus J, Woyte A, Driesen J, Belmans R. A voltage and frequency droop control method for parallel inverters. IEEE Trans Power Electron. 2007; 22: 1107-1115.

7. Guerrero JM, Matas J, de Vicuna LG, Castilla M, Miret J. Decentralized control for parallel operation of distributed generation inverters using resistive output impedance. IEEE Trans Ind Electron. 2007; 54: 994-1004.
8. Teodorescu R, Liserre M, Rodriguez P. Grid converters for photovoltaic and wind power systems. Chichester: John Wiley & Sons; 2011.
9. Zhang D. Operation of microgrid at constant frequency with a standby backup grid-forming generator. Proceedings of the 2016 IEEE International Conference on Power System Technology; 2016 September 28; Wollongong, NSW, Australia. New York: IEEE.
10. Zhang D. Operation of AC microgrids with PV panels' output power curtailment for minimizing the use of energy storage. J Energy Power Technol. 2022; 4: 008.
11. Zhang D, Fletcher J. Design and operation of an islanded microgrid at constant frequency book chapter in microgrid. Rijeka: InTechOpen; 2017.
12. Zhang D, Fletcher J. Operation of autonomous AC microgrid at constant frequency and with reactive power generation from grid-forming, grid-supporting and grid-feeding generators. Proceedings of the TENCON 2018-2018 IEEE Region 10 Conference; 2018 October 28; Jeju, South Korea. New York: IEEE.
13. Ma F, Luo A, Shuai Z, Tu C, Xiong Q. Voltage ripple analysis of simplified active power compensator for negative sequence and reactive power compensation. IET Power Electron. 2014; 7: 2582-2594.
14. Nian H, Zeng R. Improved control strategy for stand-alone distributed generation system under unbalanced and non-linear loads. IET Renew Power Gener. 2011; 5: 323-331.
15. Zhang D. Heavy mass energy storage with magnetic levitated wheels, bearings and locomotive. J Multidiscip Eng Sci Technol. 2019; 6: 10437-10442.
16. Zhang DM, Xiao D. Bi-directional heavy mass energy storage system. Canberra, Australia: Australia Patent; AU 2020202830A1; 2021.
17. Zhang DM. Massive energy storage system with distributed rotor or mover structure and transitional rotor pulse current. Alexandria, VA: USA Patent; US 11,011,967B2.
18. Zhang D. Energy buffer and other issues in heavy mass energy storage with vertical movement by linear machine. J Multidiscip Eng Sci Technol. 2019; 6: 10216-10223.
19. Zhang DM. Potential energy storage system for autonomous AC microgrid. J Multidiscip Eng Sci Technol. 2021; 8: 13836-13841.
20. Peitzke WR, Brown MB, Erdman WL, Scott RT, Moorhead WH, Douglas C, et al. Utility scale electric energy storage system. Alexandria, VA: USA patent; US 8,593,012B2.
21. Zhang D, Tseng K. A universal controller for grid-tied DC/AC converters for harnessing PV panel based solar energy and PMSG based wind energy. Proceedings of the 2015 IEEE 11th International Conference on Power Electronics and Drive Systems; 2015 June 9; Sydney, NSW, Australia. New York: IEEE.
22. Tang X, Zhang D. Islanded AC microgrid stability and feasibility analysis on VP control with estimation at constant frequency. Proceedings of the 2019 9th International Conference on Power and Energy Systems; 2019 December 10; Perth, WA, Australia. New York: IEEE.
23. Price K, Storn RM, Lampinen JA. Differential evolution: A practical approach to global optimization. Berlin: Springer Science & Business Media; 2005.
24. Qing A. Differential evolution: Fundamentals and applications in electrical engineering. Singapore: John Wiley & Sons; 2009.